

Manganese oxides synthesized via microwave-assisted hydrothermal method: phase evolution and structure refinement

Roumanos G. D. Neto

São Paulo State University

Wagner Costa Macedo (✉ wcmacedojr@gmail.com)

Sao Paulo State University <https://orcid.org/0000-0002-7793-3007>

José D. Fernandes

São Paulo State University

Agda E. S. Albas

São Paulo State University

Silvio R. Teixeira

São Paulo State University

Elson Longo

Federal University of São Carlos

Research Article

Keywords: Manganese Oxides, Hausmannite, Microwave-Assisted Hydrothermal, Rietveld Refinement, Mn₅O₈

Posted Date: December 28th, 2020

DOI: <https://doi.org/10.21203/rs.3.rs-131869/v1>

License:   This work is licensed under a Creative Commons Attribution 4.0 International License. [Read Full License](#)

Abstract

Manganese oxides were synthesized during 40 min at 140 °C via Microwave-Assisted Hydrothermal (MAH) method and treated at different temperatures in order to evaluate the phase evolution using structure refinement (Rietveld method). The samples obtained were heat treated at temperatures defined by means of thermal analysis (160 °C, 480 °C, 715 °C, 870 °C, 920 °C and 1150 °C) and analyzed by XRD, XRF, FTIR spectroscopy, Raman scattering and SEM. Structural characterizations allowed to identify five distinct phases: α - MnO_2 , Mn_3O_4 , Mn_5O_8 , $\text{Na}_2\text{Mn}_5\text{O}_{10}$ and $\text{Na}_4\text{Mn}_9\text{O}_{18}$ with weight percentages dependent on the heat treatment. The hausmannite structure (average crystallite size ranging from 28.9 nm to 99.1 nm) is present in all samples and go through various oxidation and reduction processes from 160 °C to 1150 °C without any major variation in the lattice parameters. The results presented enables a better interpretation of the thermal and structural characteristics of manganese oxides synthesized via MAH.

1 Introduction

Manganese oxides (Mn_{1-x}O , MnO_2 , Mn_2O_3 , Mn_3O_4 , Mn_5O_8 , etc.) present remarkable technological importance due to their diverse crystalline structures, many of them constituted by tunnels, that is a direct consequence of the varied oxidation states presented by Mn (2+ to 7+), which give them important applications, such as in energy storage devices, fuel cells components and supercapacitor optimization [1–5].

Mn_3O_4 (hausmannite), for example, has a spinel-like structure with a unit cell consisting of 32 oxygen atoms and 24 manganese atoms, the latter having di- and trivalent cationic states (with Mn^{2+} ions forming the tetrahedral clusters and the ions Mn^{3+} forming the octahedral clusters) [6], a particular configuration that allows this material to be used in electrochemical processes [7] and in heterogeneous photocatalysis [8]. Based on these applications, several studies report the use of hausmannite with different crystalline systems in order to photodegrade dyes such as Alizarin Yellow, Methylene Blue and Methyl Orange [9–11]. Hausmannite is also extensively used in electrochemical energy storage devices, mainly in Electrical Double-Layer Capacitors (EDLCs), replacing cobalt oxides that are more toxic and less abundant. In addition, the production of manganese oxides in their bulk form its 20 times cheaper than the production of cobalt oxides [12, 13].

Another notable stoichiometry of manganese oxides is represented by Mn_5O_8 , where the Mn cations present the states Mn^{2+} and Mn^{4+} , in addition to forming lamellar structures, such as birnessite (Mn_2O_4) [14]. Because it is a metastable structure, only recently this oxide has been used, mainly as a catalyst in denitration processes [15]. The particular mixture of valence states, with its antiferromagnetic characteristic, allows Mn_5O_8 to be used in hard disk sensors and devices based on magnetic thin films [16].

Usually, Mn_2O_3 , Mn_3O_4 , Mn_5O_8 , among others structures, are obtained through thermal decomposition of MnO_2 , particularly α - MnO_2 , where the temperatures for the various Mn oxidations depends on the characteristics of the precursor used, such as its average particle size [17, 18]. The use of thermal decomposition for manganese oxides synthesis allows to obtain a large amount of material at a reasonably low cost, however, the powder produced has a high variation in particle size, generally aggregated and without morphology control, which results in a ceramic with low density and anisotropic properties [19]. Therefore, it becomes necessary to explore other synthesis routes that allow greater control of the material's microstructure and morphology. For hausmannite, for example, several methods can be used to control the morphology of the final product, such as chemical reduction, co-precipitation,

auto-combustion, sol-gel, solid state reaction, carburization or through the conventional hydrothermal method [20–25]. Additionally, the Microwave-Assisted Hydrothermal (MAH) method is an alternative way to synthesize manganese oxides, making it possible to obtain a final material with high crystallinity, reasonable control of particle size and morphology, in addition to be environmentally friendly (the synthesis medium is not organic) and energetically viable (short synthesis times at low temperatures) [26].

This technique has gained notoriety in recent decades and is now widely used in the synthesis of advanced ceramics [27, 28]. Particularly for manganese oxides, it is likely that the first synthesis using the MAH method occurred in 2006, where Apte et al. obtained the α -MnO₂ and Mn₃O₄ phases [29]. Subsequent researches has shown that, by controlling temperature and precursors during MAH synthesis, it is possible to obtain different phases and morphologies for manganese oxide, as reported by Yu et al. on the synthesis of clew-like ϵ -MnO₂ [30] and by Li et al. on the synthesis of flower-like and nanotubes of α -MnO₂ [31]. In addition, the MAH method also makes it possible to control the amount of hausmannite nanocrystals on the surface of composites with Reduced Graphene Oxide (RGO), materials used for the development of supercapacitors [32].

Despite the better understanding of the influence that the synthesis parameters have on the characteristics of manganese oxides produced by MAH method, there are only a few studies that focus on the phase evolution of these materials from subsequent heat treatments. It was not possible to find articles that deal with the structure refinement for manganese oxides obtained by this route. Therefore, this work has as main objective the study of the MAH synthesis of manganese oxide and its crystalline phases, through the Rietveld refinement, aiming to search for a correlation between the synthesis/sintering parameters with the phase evolution after specific heat treatments.

2 Materials And Methods

For the MAH synthesis of manganese oxide, 50 mL (0.5 M) of MnCl₂·4H₂O (99%, Alphatec) and 40 mL (5.5 M) of NaOH (98%, Synth) solutions were prepared using distilled water (~ 2.5 μ S/cm) as the reaction medium. The solutions were mixed using a magnetic stirrer for 5 min, in a Teflon® vessel with maximum capacity of 100 mL, where deionized water was added until the volume of the vessel was completed. The vessel was placed in a sealed autoclave installed inside an adapted domestic microwave oven (2.45 GHz) with a fixed power of 1.0 kW and a temperature control system.

The heating rate adopted was 100 °C/min with a synthesis time of 40 min at 140 °C and a maximum pressure of 1.0 bar. After the MAH synthesis, the sample was several times washed with distilled water until the solution reached neutral pH and then the supernatant was discarded and the precipitate remained in an kiln (80 °C, 12 hs). The resulting brownish-colored powder was de-agglomerated in an agate mortar (sample MnO). Another synthesis was performed using these same parameters in order to evaluate the reproducibility of the synthesis method.

The synthesized manganese oxide (~ 12.3 mg) was submitted to thermal analysis (SDT Q-600, TA Instruments), using alumina crucibles, a heating rate of 10 °C/min, an equilibrium temperature of 30 °C, synthetic air atmosphere with 100 mL/min flow and maximum temperature of 1200 °C. The weight loss values and the maximum and/or minimum positions of the thermal processes were determined from the equipment software (Universal Analysis 2000). Then, according to the identified reactions in the thermal analysis, the MnO sample was heat treated in a low-temperature oven (EDG 3000), using alumina crucibles, with a heating rate of 10 °C/min at the following

temperatures: 160 °C, 480 °C, 715 °C, 870 °C, 920 °C and 1150 °C, during 1 h. These samples were denominated as MnO 160 °C, MnO 480 °C, MnO 715 °C, MnO 870 °C, MnO 920 °C and MnO 1150 °C, respectively.

The crystalline phases of the samples, before and after the heat treatment, were determined through an X-Ray Diffractometer - XRD - (XRD-6000, Shimadzu) at room temperature, using Cu K_{α1} ($\lambda = 1.5406 \text{ \AA}$) and Cu K_{α2} ($\lambda = 1.5444 \text{ \AA}$) radiation, divergence and reception slits of 1°, in continuous scanning mode (2°/min), 40 kV, 30 mA and 2 θ angular range from 10° to 80°. The diffraction patterns were identified using the Powder Diffraction Files (PDF) of the JCPDS-ICDD database (Joint Committee on Powder Diffraction Standards – International Center for Diffraction Data). An estimate of the average crystallite sizes of the analyzed samples was performed using the Scherrer equation, with background subtraction, K_{α2} stripping and a shape factor of 0.9.

For quantitative results on the percentages of the phases, structure refinement was performed (Rietveld method), using the GSAS software (General Structure Analysis System, available by A. C. Larson and R. B. von Dreele) [33]. This method uses the best approximation between the calculated and observed diffractograms to readjust the crystalline structure so that it is closest to the real one (best fitting approach). Specifically for the Rietveld refinement, divergence and reception slits of 0.5°, scanning speed of 0.2°/min and angular range 2 θ from 20° to 110° were adopted. Crystallography Information Framework (CIF) files from the Crystallography Open Database were also used as refinement control files.

Approximate values of the atomic percentages of the samples were obtained using an X-Ray Fluorescence spectrometer - XRF - (EDX7000, Shimadzu). A Rh cathode was used as the primary source of radiation. The scanning adopted covered characteristic energies ranging from Na to U, in qualitative-quantitative mode, at room temperature and vacuum. Biaxially oriented polyester substrates of poly(ethylene terephthalate) (boPET, Mylar®) were used and an area of approximately 80 mm² was analyzed. The sample morphologies (Au metallization) were observed using a Scanning Electron Microscope - SEM - (EVO LS 15, Zeiss).

The MnO samples were also subjected to Raman scattering via a spectrometer (inVia, Renishaw), equipped with Leica microscope, a 1800 lines/mm grid and CCD detector with scanning from 300 to 5000 cm⁻¹, 100 scans and excitation laser at 633 nm (He-Ne source). Portions of the samples were also mixed with KBr (99%, Sigma-Aldrich) in a 1:100 ratio (MnO/KBr) and uniaxially pressed (80 kN for 2 min, resulting in a 1.3 cm diameter and 3 mm thick pellets) to perform the FTIR characterization (Fourier-Transform Infrared Spectroscopy - Tensor 27, Bruker), in the range of 250 to 750 cm⁻¹, with spectral resolution of 4 cm⁻¹ and 128 scans.

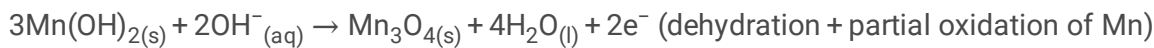
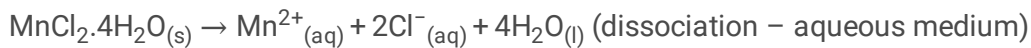
3 Results And Discussion

The XRD patterns of the MnO sample (Fig. 1) shows the presence of two phases, tetragonal Mn₃O₄ (hausmannite) (JCPDS 89-4837), with well-defined peaks, indicating high crystallinity and tetragonal α -MnO₂ (JCPDS 72-1982), which it presents low and wide peaks, indicating low crystallinity.

Apte et al. [29], using manganese nitrate, ethanolamine and ethylenediamine, obtained tetragonal phase of hausmannite with high crystallinity, even in short microwave irradiation times (1–5 min), however Li et al., using KMnO₄ and HCl as precursors, obtained birnessite-type MnO₂ and tetragonal α -MnO₂ structures, with 25 min of synthesis time and 100 °C and 140 °C, respectively, both with low crystallinity [31]. Comparing these results with the obtained phases in this work, it is very important to mention the role of precursors and synthesis parameters during the use of the MAH method in the preparation of advanced ceramics. Both in the work of Apte et al. [29] as

in the synthesis of the MnO sample, the importance of a hydrothermal solution rich in OH⁻ groups is highlighted, which usually favor the construction of the crystalline network of various ceramic oxides [34, 35], and in this case, favor the crystallization of the hausmannite structure.

When produced by the ionic liquid method, Mn₃O₄, as in this work, also has a small MnO₂ impurity, suggesting that the synthesis environment where there is a high concentration of hydroxyls is adequate to stabilize manganese ions and promote the nucleation of Mn₃O₄ but can result in spurious phases [6, 36]. After the precursors dissociation and the sodium chloride and manganese hydroxide precipitation, partial oxidation of Mn (Mn²⁺ to Mn³⁺) occurs, with the interaction with hydroxyls, resulting in formation of Mn₃O₄ structure. It is assumed that the formation of a small portion of α-MnO₂ is the result of a charge imbalance promoted by the insertion of Na⁺ ions (from NaOH mineralizer) into the interstices of the synthesized material, since hausmannite has a reversible intercalation capacity for alkali metal ions [37–39]. These chemical reactions involved in the construction of the Mn₃O₄ crystalline network can be summarized as follows:



It is known that phase transformations in relation to the temperature variation in manganese oxides depends on the used precursors, stoichiometry, particle size and the morphology of the synthesized materials [6]. The transition temperature from the Mn₃O₄ phase to Mn₅O₈ metastable phase, for example, has a range of up to 130 °C (from 350 °C to 480 °C), depending mainly on the used precursors and the particle size of the treated material [10, 40, 41]. Therefore, to evaluate these phase transformations specifically for the manganese oxide synthesized via MAH, the MnO sample was subjected to thermal analysis.

The thermal analysis up to 1200 °C (thermogravimetry and differential scanning calorimetry) of the MnO sample is shown in Fig. 2. Two endothermic reactions are observed up to approximately 117 °C, accompanied by a weight loss of 1.34%, which are associated with the desorption of molecules on the sample surface, usually water molecules, a common phenomenon that occurs in this type of oxide [42].

The relatively intense exothermic reaction at 204 °C and the low intensity endothermic reaction at approximately 355 °C are most likely related to the reduction and oxidation processes of both α-MnO₂ and Mn₃O₄, respectively [43]. Thermal oxidation processes are usually accompanied by weight losses, resulting from the interaction of the treated sample with the furnace atmosphere, this weight loss in the 117 °C-454 °C range was approximately 1.60% and may also be related to the desorption of hydroxyls still present on the particle surface and the loss of structural water [44]. The characteristic weight gain (0.15%) between 454 °C and 524 °C can be related to the manganese oxide reduction, particularly during the transformation of Mn₅O₈ to Mn₂O₃ and Mn₃O₄, where there is a total reduction of Mn⁴⁺ ions to Mn³⁺ [45]. The existence of the Mn₅O₈ metastable phase in this temperature range can be confirmed through the XRD patterns of the MnO 480 °C sample (Fig. 3 (c)).

Then, between 524 °C and 715 °C, the reactions indicate the conversion of Mn₂O₃ phase to Mn₃O₄ (peaked at 657 °C) and O₂ release, resulting in a considerable weight loss, around 2.08%. Finally, still in Fig. 2, from 715 °C to 1200 °C, several low intensity reactions are noticed, most likely related to the movement of ions such as Na⁺ in the hausmannite network. Of these low intensity reactions, only the peaks around 975 °C stand out, where there is a new conversion of the Mn₃O₄ to Mn₂O₃ [46], it is more liked that in this work this temperature stands belows 975 °C (from 870 °C), and is represented by a slow reaction, since there is no prominent peak of 700 °C up to 1000 °C. In addition, two reactions stand out in the range 715 °C-1200 °C, one around 1052 °C [45], characteristic of the second conversion from the Mn₂O₃ to Mn₃O₄ phase, which in this case is represented by a rapid endothermic reaction and another around 1175 °C, characteristic of the transformation from the tetragonal Mn₃O₄ to cubic Mn₃O₄ [47]. In this same range, there is a weight loss of approximately 2.31%, also related to the release of O₂. Considerations regarding the thermal analysis of the MnO sample are summarized in Table 1.

Table 1
– Thermal phenomena for the MnO sample in the range of 30 °C to 1200 °C.

Temperature Range (°C)	Thermal Phenomena	Phase Transformation
30–117	Desorption of molecules, such as water, from the surface of α-MnO ₂ and Mn ₃ O ₄ particles.	-
117–454	Reduction of α-MnO ₂ (204 °C) and oxidation of Mn ₃ O ₄ (355 °C). Structural water removal. Hydroxyl desorption.	α-MnO ₂ → Mn ₃ O ₄ Mn ₃ O ₄ → Mn ₅ O ₈
454–524	Reduction of Mn ₅ O ₈ .	Mn ₅ O ₈ → Mn ₂ O ₃ Mn ₅ O ₈ → Mn ₃ O ₄
534–715	Oxidation of Mn ₂ O ₃ (657 °C). O ₂ release.	Mn ₂ O ₃ → Mn ₃ O ₄
715–1200	Ionic movement in the Mn ₃ O ₄ network. Reduction of Mn ₃ O ₄ . Oxidation of Mn ₂ O ₃ (1052 °C). Transformation of the tetragonal Mn ₃ O ₄ phase to cubic Mn ₃ O ₄ (1175 °C). O ₂ release.	Mn ₃ O ₄ ↔ Mn ₂ O ₃ Tetragonal Mn ₃ O ₄ → Cubic Mn ₃ O ₄

Figure 3 shows the XRD patterns of MnO sample compared with the diffraction patterns of the samples treated at 160 °C, 480 °C, 715 °C, 870 °C, 920 °C and 1150 °C, for 1 h. These temperatures were set to analyze the sample structure right after a weight loss range indicated by the thermogram. As expected, for MnO 160 °C sample (Fig. 3 (b)), α-MnO₂ and Mn₃O₄ phases are still present, however, the peaks located at 19° and 25° referring to α-MnO₂ phase are less intense and broader compared to MnO sample, indicating long-range disorder and/or smaller particle size of α-MnO₂ phase around 160 °C. According to Fig. 2, its oxidation (α-MnO₂ → Mn₃O₄) will only occur at 204 °C. The diffractogram of MnO 480 °C sample indicates the existence of two distinct phases, Mn₃O₄, well

crystallized and monoclinic Mn_5O_8 (JCPDS 39-1218), with low crystallinity. Also according to the thermal analysis, the oxidation process $\text{Mn}_3\text{O}_4 \rightarrow \text{Mn}_5\text{O}_8$ starts at approximately 355 °C, however, at 480 °C these two phases coexist, due to the consequent reduction of metastable Mn_5O_8 , which starts around 454 °C [45].

From MnO 715 °C sample, the only stoichiometry of the manganese oxide present is hausmannite, although there are several phase transformations at intermediate temperatures, which means that the selected temperatures (except in 480 °C) coincide with the stability temperatures of Mn_3O_4 . It is interesting to observe the appearance of the monoclinic $\text{Na}_2\text{Mn}_5\text{O}_{10}$ phase (JCPDS 27-749), verified from the peaks around 17°, 19°, 30° and 37°, in MnO 715 °C sample (Fig. 3 (d)), and orthorhombic $\text{Na}_4\text{Mn}_9\text{O}_{18}$ phase (JCPDS 27-750), verified from the peak around 38°, in the samples MnO 870 °C and MnO 920 °C (Fig. 3 (e) and (f)). The presence of these manganese oxides with sodium is a clear indication that, even before heat treatments, Na^+ ions are inserted in the some sites of the synthesized material network. As previously mentioned, the existence of these doped ions probably resulted in the unbalance of charges that allowed the formation of the residual $\alpha\text{-MnO}_2$ right after the MAH synthesis, as well as in low intensity endothermic reactions in the 715 °C-1200 °C range, which most likely are related to the crystallization of $\text{Na}_2\text{Mn}_5\text{O}_{10}$ and $\text{Na}_4\text{Mn}_9\text{O}_{18}$ phases which, in MnO 1150 °C sample (Fig. 3 (g)), no longer exist – that is the only sample that presents a single crystalline phase represented by Mn_3O_4 , still tetragonal.

Table 2 shows the results of the semi-quantitative chemical analysis via XRF spectrometry, performed in a vacuum chamber in qualitative-quantitative mode, of untreated and thermally treated MnO samples. The atomic percentages of the samples vary from 98.36% to 98.76% (mean value of 98.50%) for Mn and from 1.24% to 1.79% (mean value of 1.50%) for Na, these values are within the equipment error (+/- 0.5%). These results are consistent with the observation of $\text{Na}_2\text{Mn}_5\text{O}_{10}$ and $\text{Na}_4\text{Mn}_9\text{O}_{18}$ phases in the diffractograms and are sufficient to confirm the presence of interstitial Na in the samples where there is no crystallization of the manganese and sodium oxides. As mentioned earlier, hausmannite works as an alkali metal ion intercalation compound, so it is understandable that, from the MAH solution rich in Na^+ , there is insertion of this ion in the network of the synthesized material. The most used electrolyte in Mn_3O_4 -based capacitive systems, are aqueous solutions of Na_2SO_4 , several studies report the formation of $\text{Na}_x\text{Mn}_y\text{O}_6$ species from these solutions and these oxides are responsible for the pseudocapacitive behavior of Mn_3O_4 [37, 38, 48].

In addition, Fig. 4 shows the XRD patterns of the manganese oxide replicated samples, the results are essentially the same, indicating reproducibility of the synthesis method.

Table 2

– XRF elementary analysis of MnO, MnO 160 °C, MnO 480 °C, MnO 715 °C, MnO 870 °C, MnO 920 °C and MnO 1150 °C samples.

Sample	Atomic Percentage (at%)	
	Mn	Na
MnO	98.39	1.61
MnO 160 °C	98.56	1.44
MnO 480 °C	98.64	1.36
MnO 715 °C	98.48	1.52
MnO 870 °C	98.30	1.70
MnO 920 °C	98.36	1.64
MnO 1150 °C	98.76	1.24
Mean Value	98.50	1.50

Table 3 shows the average crystallite sizes, calculated from the most intense peak of each identified phase, for MnO samples and their replicates. For both sets of samples, it is possible to observe that α -MnO₂ phase is the one with the lowest values for the average sizes (mean value of 20.6 nm) and Mn₃O₄ phase is the one with the largest variations for these values in relation to heat treatment, ranging from 28.9 nm to 99.1 nm. The crystallites for Na₄Mn₉O₁₈ phase are slightly larger than those presented by Na₂Mn₅O₁₀ phase (mean values of 28.2 nm and 51.8 nm, respectively), which may be associated with the higher theoretical volume of Na₄Mn₉O₁₈ phase. Furthermore, for comparison, Rani et al. [12] report the average crystallite sizes of 28.3 nm and 56.6 nm for the Mn₃O₄ phase synthesized by co-precipitation and sol-gel, respectively. Liu et al. [32] obtained Mn₃O₄/RGO nanocomposites by MAH method with reduced crystallite size (around 18.4 nm).

Table 3

– Average crystallite sizes of MnO, MnO 160 °C, MnO 480 °C, MnO 715 °C, MnO 870 °C, MnO 920 °C and MnO 1150 °C samples and its respective replicas.

Sample	Average Crystallite Sizes (nm)				
	α -MnO ₂	Mn ₃ O ₄	Mn ₅ O ₈	Na ₂ Mn ₅ O ₁₀	Na ₄ Mn ₉ O ₁₈
MnO	20.9	80.5	-	-	-
MnO 160 °C	19.6	67.2	-	-	-
MnO 480 °C	-	28.9	32.1	-	-
MnO 715 °C	-	77.5	-	26.2	-
MnO 870 °C	-	99.1	-	-	48.6
MnO 920 °C	-	43.5	-	-	57.2
MnO 1150 °C	-	46.5	-	-	-
Sample (Replica)	Average Crystallite Sizes (nm)				
	α -MnO ₂	Mn ₃ O ₄	Mn ₅ O ₈	Na ₂ Mn ₅ O ₁₀	Na ₄ Mn ₉ O ₁₈
MnO	21.3	72.5	-	-	-
MnO 160 °C	20.5	70.7	-	-	-
MnO 480 °C	-	31.9	33.3	-	-
MnO 715 °C	-	72.5	-	30.2	-
MnO 870 °C	-	84.2	-	-	48.2
MnO 920 °C	-	44.6	-	-	53.4
MnO 1150 °C	-	47.8	-	-	-

The main vibrational modes for MnO samples, determined by FTIR characterization, are shown in Fig. 5, in the range 250–750 cm⁻¹. Four broad bands are initially observed for all samples, indicating overlapping of vibrational modes and possible symmetry breaks [49–53] in the MnO_x clusters which may be related to the presence of Na in these materials, as evidenced by XRF (Table 2). A wide band around 300 cm⁻¹ can be attributed to external vibrations caused by translational movement from the MnO₆ cluster [31, 53]. It is also possible to notice the characteristic vibrational coupling mode of the Mn–O stretch at the tetrahedral and octahedral sites of Mn₃O₄ around 370 cm⁻¹ [12, 49], suggesting that all samples have the hausmannite phase, as shown in the diffractograms. A clear vibrational separation in this band (372 cm⁻¹ and 381 cm⁻¹) is observed for MnO 715 °C, MnO 870 °C and MnO 920 °C samples, which are the same samples that presents the sodium-manganese oxide phase crystallization. It is likely that the orderly presence of Na⁺ around the MnO₄ and MnO₆ clusters results in the Mn²⁺ and Mn³⁺ ions displacement, resulting in the appearance of the new band.

The absorption band centered at 470 cm⁻¹ is characteristic of the stretching vibrations of the Mn³⁺–O bonds in the octahedral sites of the Mn₃O₄ phase [54]. When there is an excess of vacancies in this structure, Mn³⁺ to Mn⁴⁺ oxidation usually occurs and this causes this band to move to highest wavenumbers, characterizing the Mn⁴⁺–O

bond [54]. It is possible to observe this displacement for the MnO 480 °C sample, where the band displaced to 482 cm^{-1} , however, this is the result of the Mn^{4+} ions in Mn_5O_8 phase, formed from the heat treatment.

A wide band centered at approximately 598 cm^{-1} (Mn–O bending of the tetrahedral site together with distortion vibration of Mn–O in the octahedral site [55]), presents another remarkable separation (595 cm^{-1} and 600 cm^{-1}) only for the samples MnO 715 °C, MnO 870 °C and MnO 920 °C, one more indicative of the distortion of MnO_4 and MnO_6 clusters, resulting from the presence of Na. It is worth mentioning that, although the monoclinic $\text{Na}_2\text{Mn}_5\text{O}_{10}$ and orthorhombic $\text{Na}_4\text{Mn}_9\text{O}_{18}$ are known and currently explored for use in ionic sodium batteries [1, 51], it was not possible to find articles that deal with the specific vibrational modes for these materials. Additionally, it is important to note that the decrease in the absorption bands is related to the lower crystallinity/quality of the material [50], this occurs mainly in the MnO 1150 °C sample, in agreement with the less intense diffraction patterns for this sample observed in Fig. 3 (g).

To complement the considerations made about the vibrational modes identified, Fig. 6 shows the Raman scattering for the MnO samples in the ranges $300\text{--}1200\text{ cm}^{-1}$ and $300\text{--}5000\text{ cm}^{-1}$ (Fig. 6 (a) and (b), respectively). It is possible to observe that, in all the analyzed ranges, there is an evident decrease in the background in relation to the heat treatment temperature that which supposedly increases the size of the particles with increasing temperature. This is assumed to be related to luminescent emissions, which are highly dependent on particle size [56, 57]. J. Wang et al. [58] report two main absorption regions for hausmanite nanoparticles, a larger one around 450 nm and a smaller one around 650 nm, so it is consistent to assume that there is a partial absorption of the excitation laser used in Raman scattering (633 nm) and this is evident from the observed luminescent emissions (wide bands in the infrared region, from 300 cm^{-1} to 5000 cm^{-1}). This same absorption of the excitation laser and consequent emission in the infrared region was observed by C. B. Azzoni et al. [59] for Mn_5O_8 powder.

According to Fig. 6 it is possible to assume that with the increase of temperature, there is particle growth and consequent decrease in the luminescent emission. Therefore, the vibrational modes for most samples are overlapped by these emissions, which makes it difficult to interpret the results properly. In addition, MnO 480 °C sample has two prominent luminescent emission intervals, around 2150 cm^{-1} and 3750 cm^{-1} , which can be attributed to Mn_5O_8 and Mn_3O_4 which together are only present in this sample.

The hausmannite vibrational modes are only evident in the spectra of the MnO 920 °C and MnO 1150 °C samples (Fig. 6 (a)), in these samples the fluorescence emissions are not able to overlap the vibrational modes in low wavenumbers, due to the larger particle sizes which suppress emissions. The 319 cm^{-1} and 373 cm^{-1} bands are assigned to the T_{2g} vibrational mode of tetragonal Mn_3O_4 [12] and 647 cm^{-1} (MnO 920 °C) and 657 cm^{-1} (MnO 1150 °C) bands can be assigned to A_{1g} mode, referring to Mn–O bonds (stretching) of the hausmannite divalent Mn ions with tetrahedral coordination [57]. The widening of this band and the consequent displacement to smaller wavenumbers from the MnO 1150 °C sample to the MnO 920 °C, is probably linked to the smaller particle size and the presence of the $\text{Na}_4\text{Mn}_9\text{O}_{18}$ phase (Fig. 3) in the MnO 920 °C sample.

To estimate the percentage and network parameters of the identified phases, structure refinement of the samples synthesized via MAH and treated was carried out using the Rietveld method. Their respective diffractograms are shown in Figs. 7 and 8 and the results are summarized in Table 4. Tetragonal Mn_3O_4 (CIF 1514115) was identified for all temperatures, its portion in the MnO and MnO 160 °C samples approaches 100% (despite the existence of the tetragonal $\alpha\text{-MnO}_2$ phase in these samples, it was not taken into account in the refinement due to wide and low

intensity peaks that lead to divergency), decreases to 5.53% in 480 °C, due to the transformation of hausmannite in the metastable phase (monoclinic Mn_5O_8 - CIF 1514100) and, in the following temperatures, remains above 89%, ending in 100% for MnO 1150 °C sample.

It is interesting to point out the percentages of the monoclinic $\text{Na}_2\text{Mn}_5\text{O}_{10}$ (CIF 1528293) and orthorhombic $\text{Na}_4\text{Mn}_9\text{O}_{18}$ (CIF 2017971) phases apparent only in the samples MnO 715 °C, MnO 870 °C and MnO 920 °C, these values vary from 1.14% of $\text{Na}_2\text{Mn}_5\text{O}_{10}$ (MnO 715 °C sample), to 9.78% and 10.64% of $\text{Na}_4\text{Mn}_9\text{O}_{18}$ in the MnO 870 °C and MnO 920 °C samples, respectively.

Table 4

– Phase percentages, lattice parameters and convergence parameters of MnO, MnO 160 °C, MnO 480 °C, MnO 715 °C, MnO 870 °C, MnO 920 °C and MnO 1150 °C samples.

Sample	Phase Percentage and Lattice Parameters						R _{WP} (%)	R _{EXP} (%)	χ ²	
MnO	Tetragonal Mn ₃ O ₄ (~ 100 wt%)*						3.121	1.766	1.330	
	a,b (Å)		c (Å)		V (Å ³)					
	5.7698		9.4521		314.67					
MnO 160 °C	Tetragonal Mn ₃ O ₄ (~ 100 wt%)*						3.516	2.587	1.833	
	a,b (Å)		c (Å)		V (Å ³)					
	5.77033		9.4654		315.17					
MnO 480 °C	Tetragonal Mn ₃ O ₄ (5.53 wt%)			Monoclinic Mn ₅ O ₈ (94.47 wt%)			10.053	4.274	5.533	
	a,b (Å)	c (Å)	V (Å ³)	a (Å)	b (Å)	c (Å)				V (Å ³)
	5.7602	9.4885	314.83	10.4530	5.7560	4.8734				276.13
MnO 715 °C	Tetragonal Mn ₃ O ₄ (98.86 wt%)			Monoclinic Na ₂ Mn ₅ O ₁₀ (1.14 wt%)			4.388	2.601	2.827	
	a,b (Å)	c (Å)	V (Å ³)	a (Å)	b (Å)	c (Å)				V (Å ³)
	5.7626	9.4675	314.40	8.9605	11.0579	2.8053				277.96
MnO 870 °C	Tetragonal Mn ₃ O ₄ (90.22 wt%)			Orthorhombic Na ₄ Mn ₉ O ₁₈ (9.78 wt%)			3.723	2.563	2.110	
	a,b (Å)	c (Å)	V (Å ³)	a (Å)	b (Å)	c (Å)				V (Å ³)
	5.7633	9.4684	314.50	9.0986	26.1584	2.8254				672.47
MnO 920 °C	Tetragonal Mn ₃ O ₄ (89.36 wt%)			Orthorhombic Na ₄ Mn ₉ O ₁₈ (10.64 wt%)			3.865	2.558	2.283	
	a,b (Å)	c (Å)	V (Å ³)	a (Å)	b (Å)	c (Å)				V (Å ³)
	5.7631	9.4677	314.45	9.1049	26.1970	2.8255				673.94
MnO 1150 °C	Tetragonal Mn ₃ O ₄ (100 wt%)						3.249	2.674	1.476	
	a,b (Å)		c (Å)		V (Å ³)					
	5.7648		9.4693		314.70					

* The α-MnO₂ phase was not considered in the refinement due to its wide and low intensity peaks, with no possibility of convergence if it is taken into account.

Despite the atomic percentage of Na being around 1.50% in the studied samples, the high percentage observed for Na₄Mn₉O₁₈ phase is related to the high volume of the Na₄Mn₉O₁₈ unit cell (which ranges from 672.47 Å³ to 673.94

\AA^3) in relation to the volume of Mn_3O_4 (which ranges from 314.40 \AA^3 to 315.17 \AA^3). In addition, the refinements showed great convergent parameters (R_{WP} , R_{EXP}) and goodness of fit (χ^2): 1.330 (MnO), 1.833 (MnO 160 °C), 5.533 (MnO 480 °C), 2.827 (MnO 715 °C), 2.110 (MnO 870 °C), 2.283 (MnO 920 °C) and 1,476 (MnO 1150 °C), indicating a good approximation of the observed results in comparison with those calculated.

Finally, to assess the influence of the synthesis method and thermal treatment on the morphology of the material produced, the samples were characterized by SEM (Fig. 9). According to the synthesis method and the precursors used, the same compound can present different morphologies, therefore, it is important to analyze the microscopy of samples synthesized by MAH. The samples MnO and MnO 160 °C presented many particles with well-defined edges, some rods with a triangular section, with many particles with different morphologies and uniform size (Fig. 9 (a) and (b)). Such microscopies suggest the crystalline hausmannite, according to Rani et al., Liu et al. and Yang et al. [12, 32, 60]. The MnO 480 °C sample also showed particles with well-defined edges, but more agglomerated, which can characterize the Mn_5O_8 phase (Fig. 9 (c)), as suggested by Gao et al. and Aghazadeh et al. [13, 14].

The MnO 715 °C sample (Fig. 9 (d)) presents particles with different morphologies and uniform size. One of these morphologies is characterized by the presence of particles in the form of needles or rods, which suggest the formation of $\text{Na}_2\text{Mn}_5\text{O}_{10}$, according to Liu et al. and Tsuda et al. [1, 61]. Both authors suggest the formation of romanechite with sodium. The samples MnO 870 °C and MnO 920 °C are similar, they show bars with hexagonal base, particles with different morphologies of different sizes, agglomerates and spheroidal particles (Fig. 9 (e) and (f)). Such spheroidal formations, according to Ta et al. [51], suggest the $\text{Na}_4\text{Mn}_9\text{O}_{18}$ phase, agreeing with the diffractograms presented.

The MnO 1150 °C sample has particles with smooth surfaces. The morphology and size were neither defined nor uniform, although some particles have an octahedral shape with the chamfered corners (Fig. 9 (g)). For this temperature, it can be observed that the particles greatly increase their sizes in relation to the other samples which agrees with the assumptions made for the luminescent emissions observed from the Raman scattering (Fig. 6): the increase in the heat treatment temperature results in an increase in the particle size, which reduces the observed luminescent emission.

4 Conclusions

The Microwave-Assisted Hydrothermal (MAH) method proved to be effective in the synthesis of manganese oxide, mainly with the hausmannite phase (Mn_3O_4), in a simplified, reproductive and fast way compared to other synthesis methods found in the literature. It was possible to observe a cyclical evolution of the hausmannite structure from room temperature to 1150 °C where, in the initial temperatures (room and 160 °C), the tetragonal Mn_3O_4 phase with traces of $\alpha\text{-MnO}_2$ was identified. Around 480 °C, there was almost total transformation of the Mn_3O_4 phase (5.53%) into Mn_5O_8 (94.47%). At subsequent temperatures, it is possible to notice that the synthesized material acted as a Na intercalation compound, because at 715 °C, there was crystallization of $\text{Na}_2\text{Mn}_5\text{O}_{10}$ phase (1.14%), still with the presence of hausmannite (98.86%) and at 870 °C/920 °C, the crystallization of the $\text{Na}_4\text{Mn}_9\text{O}_{18}$ phase (9.78%/10.64%, together with 90.22% and 89.36% of Mn_3O_4 , respectively), to finally culminate in the single-phase sample (100% Mn_3O_4), treated at 1150 °C. From Raman scattering it was possible to observe that there is luminescent emission (at 633 nm excitation) mainly for samples treated at lower

temperatures, with smaller particle sizes. The results presented allowed a better interpretation of the chemical, thermal and structural characteristics of manganese oxide samples synthesized via MAH.

Declarations

Acknowledgements

This work was supported by FAPESP/CEPID [2013/07296-2] and CNPq [573636/2008-7].

References

1. Liu S, Fan CZ, Zhang Y, *et al.* Low-temperature synthesis of $\text{Na}_2\text{Mn}_5\text{O}_{10}$ for supercapacitor applications. *J Power Sources* 2011, **196**: 10502-10506.
2. Wang G, Zhang L, Zhang J, A review of electrode materials for electrochemical supercapacitors. *Chem Soc Rev* 2012, **41**: 797-828.
3. Robinson DM, Go YB, Mui M, *et al.* Photochemical water oxidation by crystalline polymorphs of manganese oxides: structural requirements for catalysis. *J Am Chem Soc* 2013, **135**: 3494-3501.
4. Manigandan R, Giribabu K, Munusamy S, *et al.* Manganese sesquioxide to trimanganese tetroxide hierarchical hollow nanostructures: effect of gadolinium on structural, thermal, optical and magnetic properties. *Cryst Eng Comm* 2015, **17**: 2886-2895.
5. Sarac FE, Unal U, Electrochemical-hydrothermal synthesis of manganese oxide films as electrodes for electrochemical capacitors. *Electrochim Acta* 2015, **178**: 199-208.
6. Sukhdev A, Challa M, Narayani L, *et al.* Synthesis, phase transformation, and morphology of hausmannite Mn_3O_4 nanoparticles: photocatalytic and antibacterial investigations. *Heliyon* 2020, **6**: e03245.
7. Ashoka S, Nagaraju G, Chandrappa GT, Reduction of KMnO_4 to Mn_3O_4 via hydrothermal process. *Mater Lett* 2010, **64**: 2538-2540.
8. Xu Y, Guo X, Zha F, *et al.* Efficient photocatalytic removal of orange II by a $\text{Mn}_3\text{O}_4\text{-FeS}_2/\text{Fe}_2\text{O}_3$ heterogeneous catalyst. *J Environ Manage* 2020, **253**: 109695.
9. Ahmed KAM, Huang K, Formation of Mn_3O_4 nanobelts through the solvothermal process and their photocatalytic property. *Arab J Chem* 2019, **12**: 429-439.
10. Ullah AKM, Akter KK, Tareq F, Oxidative degradation of methylene blue using Mn_3O_4 nanoparticles. *Water Cons Sci Eng* 2017, **1**: 249-256.
11. Dong C, Liu X, Guan H, *et al.* Combustion synthesized hierarchically porous Mn_3O_4 for catalytic degradation of methyl orange. *Can J Chem Eng* 2017, **95**: 643-647.
12. Rani RJ, Ravina M, Ravi G, *et al.* Synthesis and characterization of hausmannite (Mn_3O_4) nanostructures. *Brit Cer Pr* 2018, **11**: 28-36.
13. Gao J, Lowe MA, Abruna HD, Sponge like nanosized Mn_3O_4 as a high-capacity anode material for rechargeable lithium batteries. *Chem Mater* 2011, **23**: 3223-3227.
14. Aghazadeh M, Electrochemical preparation and characterization of Mn_5O_8 nanostructures. *J Nanostruct* 2018, **8**: 67-74.

15. Qi K, Xie J, Fang D, *et al.* Mn₅O₈ nanoflowers prepared via a solvothermal route as efficient denitration catalysts. *Mater Chem Phys* 2018, **209**: 10-15.
16. Punnoose A, Magnone H, Seehra MS, Synthesis and antiferromagnetism of Mn₅O₈. *IEEE T Magn* 2001, **37**: 2150-2152.
17. Dai Y, Wang K, Xie J, From spinel Mn₃O₄ to layered nanoarchitectures using electrochemical cycling and the distinctive pseudocapacitive behavior. *Appl Phys Lett* 2007, **90**: 104102.
18. Komaba S, Tsuchikawa T, Ogata A, *et al.* Nano-structured birnessite prepared by electrochemical activation of manganese(III)-based oxides for aqueous supercapacitors. *Electrochim Acta* 2012, **59**: 455-463.
19. Davar F, Niasari MS, Mir N, *et al.* Thermal decomposition route for synthesis of Mn₃O₄ nanoparticles in presence of a novel precursor. *Polyhedron* 2010, **29**: 1747-1753.
20. Igor D, Tetyana K, Galina V, *et al.* La_{0.7}Sr_{0.3}MnO₃ nanopowders: synthesis of different powders structures and real magnetic properties of nanomanganites. *Mater Charact* 2013, **82**: 140-145.
21. Pei LZ, Yang Y, Yuan CZ, *et al.* A simple route to synthesize manganese germanate nanorods. *Mater Charact* 2011, **62**: 555-562.
22. Bernier N, Xhoffer C, Van de Putte T, *et al.* Structure analysis of aluminium silicon manganese nitride precipitates formed in grain-oriented electrical steels. *Mater Charact* 2013, **86**: 116-126.
23. Conceição L, Silva CRB, Ribeiro NFP, *et al.* Influence of the synthesis method on the porosity, microstructure and electrical properties of La_{0.7}Sr_{0.3}MnO₃ cathode materials. *Mater Charact* 2009, **60**: 1417-1423.
24. Ducmana V, Korata L, Legata A, *et al.* X-ray micro-tomography investigation of the foaming process in the system of waste glass-silica mud-MnO₂. *Mater Charact* 2013, **86**: 316-321.
25. Zheng JX, Yuan R, Luo RC, *et al.* Atomic imaging of the coherent interface between orientedly-attached Mn₃O₄ nanoparticles. *Mater Charact* 2016, **117**: 144-148.
26. Meng LY, Wang B, Ma MG, *et al.* The progress of microwave-assisted hydrothermal method in the synthesis of functional nanomaterials. *Mater Today Chem* 2016, **1-2**: 63-83.
27. Zhu YJ, Chen F, Microwave-assisted preparation of inorganic nanostructures in liquid phase. *Chem Rev* 2014, **114**: 6462-6555.
28. Komarneni S, Nanophase materials by hydrothermal, microwave-hydrothermal and microwave-solvothermal method. *Curr Sci* 2003, **85**: 1730-1734.
29. Apte SK, Naik SD, Sonawane RS, *et al.* Nanosize Mn₃O₄ (Hausmannite) by microwave irradiation method. *Mater Res Bull* 2006, **41**: 647-654.
30. Yu P, Zhang X, Wang D, *et al.* Shape-controlled synthesis of 3D hierarchical MnO₂ nanostructures for electrochemical supercapacitors. *Cryst Growth Des* 2009, **9**: 528-533.
31. Li Y, Wang J, Zhang Y, *et al.* Facile controlled synthesis and growth mechanisms of flower-like and tubular MnO₂ nanostructures by microwave-assisted hydrothermal method. *J Colloid Interf Sci* 2012, **369**: 123-128.
32. Liu CL, Chang KH, Hu CC, *et al.* Microwave-assisted hydrothermal synthesis of Mn₃O₄/reduced graphene oxide composites for high power supercapacitors. *J Power Sources* 2012, **217**: 184-192.
33. Larson, AC, Von Dreele, RB, General structure analysis system (GSAS) program. Los Alamos, NM, Rep. N°. LAUR 86-748, Los Alamos National Laboratory, University of California, California, USA, 2004.

34. Bregadiolli BA, Fernandes SL, Graeff CFO, Easy and fast preparation of TiO₂-based nanostructures using microwave assisted hydrothermal synthesis. *Mat Res* 2017, **20**: 912-919.
35. Meng LY, Wang B, Ma MG, *et al.* The progress of microwave-assisted hydrothermal method in the synthesis of functional nanomaterials. *Mater Today Chem* 2016, **1-2**: 63-83.
36. Bussamara R, Melo WW, Scholten JD, *et al.* Controlled synthesis of Mn₃O₄ nanoparticles in ionic liquids. *Dalton Trans* 2013, **42**: 14473-14478.
37. Dubal DP, Jagadale AD, Lokhande CD, Big as well as light weight portable, Mn₃O₄ based symmetric supercapacitive devices: fabrication, performance evaluation and demonstration. *Electrochim Acta* 2012, **80**: 160-170.
38. Raj BGS, Asiri AM, Wu JJ, *et al.* Synthesis of Mn₃O₄ nanoparticles via chemical precipitation approach for supercapacitor application. *J Alloys Compd* 2015, **636**: 234-240.
39. Raj BGS, Ramprasad RNR, Asiri AM, *et al.* Ultrasound assisted synthesis of Mn₃O₄ nanoparticles anchored graphene nanosheets for supercapacitor applications. *Electrochim Acta* 2015, **156**: 127-137.
40. Lee JH, Sa YJ, Kim TK, *et al.* A transformative route to nanoporous manganese oxides of controlled oxidation states with identical textural properties. *J Mater Chem A* 2014, **2**: 10435-10443.
41. Baykal A, Köseoglu Y, Senel M, Low temperature synthesis and characterization of Mn₃O₄ nanoparticles. *Cent Eur J Chem* 2007, **5**: 169-176.
42. Rakitskaya T, Truba A, Dzhyga G, *et al.* Water vapor adsorption by some manganese oxide forms. *Colloids Interfaces* 2018, **2**: 1-10.
43. Zaki MI, Hasan MA, Pasupulety L, *et al.* Thermochemistry of manganese oxides in reactive gas atmospheres: probing redox compositions in the decomposition course MnO₂ → MnO. *Thermochim Acta* 1997, **303**: 171-181.
44. Lagauche M, Larmier K, Jolimaitre E, *et al.* Thermodynamic characterization of the hydroxyl group on the γ -alumina surface by the energy distribution function. *J Phys Chem C* 2017, **121**: 16770-16782.
45. Pike J, Hanson J, Zhang L, *et al.* Synthesis and redox behavior of nanocrystalline hausmannite (Mn₃O₄). *Chem Mater* 2007, **19**: 5609-5616.
46. Amankwah RK, Pickles CA, Thermodynamic, thermogravimetric and permittivity studies of hausmannite (Mn₃O₄) in air. *J Therm Anal Calorim* 2009, **98**: 849-853.
47. McMurdie HF, Sullivan BM, Mauer FA, High-temperature X-ray study of the system Fe₃O₄-Mn₃O₄. *J Res Natl Bur Stan (U.S.)* 1950, **45**: 35-41.
48. Shen KY, Lengyel M, Wang L, *et al.* Spray pyrolysis and electrochemical performance of Na_{0.44}MnO₂ for sodium-ion battery cathodes. *MRS Commun* 2017, **7**: 74-77.
49. Li Y, Li XM, Facile treatment of wastewater produced in Hummer's method to prepare Mn₃O₄ nanoparticles and study their electrochemical performance in an asymmetric supercapacitor. *RSC Adv* 2013, **3**: 2398-2403.
50. Gund GS, Dubal DP, Patil BH, *et al.* Enhanced activity of chemically synthesized hybrid graphene oxide/Mn₃O₄ composite for high performance supercapacitors. *Electrochim Acta* 2013, **92**: 205-2015.
51. Ta AT, Nguyen VN, Nguyen TTO, *et al.* Hydrothermal synthesis of Na₄Mn₉O₁₈ nanowires for sodium ion batteries. *Ceram Int* 2019, **45**: 17023-17028.

52. Wu Z, Yu K, Huang Y, *et al.* Facile solution-phase synthesis of γ - Mn_3O_4 hierarchical structures. *Chem Cent J* 2007, **1**: 8.
53. Gao T, Fjellvag H, Norby P, *et al.* A comparison study on Raman scattering properties of alpha- and beta- MnO_2 . *Anal Chim Acta* 2009, **648**: 235-239.
54. Bose VC, Biju V. Structure, cation valence states and electrochemical properties of nanostructured Mn_3O_4 . *Mater Sci Semicond Process* 2015, **35**: 1-9.
55. Sackey J, Akbari M, Morad R, *et al.* Molecular dynamics and bio-synthesis of phoenix dactylifera mediated Mn_3O_4 nanoparticles: electrochemical application. *J Alloy Compd* 2021, **854**: 156987.
56. Toufiq AM, Wang F, Javed QUA, *et al.* Synthesis, characterization and photoluminescent properties of 3D nanostructures self-assembled with Mn_3O_4 nanoparticles. *Mater Express* 2014, **4**: 258-262.
57. Han YF, Chen F, Zhong Z, *et al.* Controlled synthesis, characterization, and catalytic properties of Mn_2O_3 and Mn_3O_4 nanoparticles supported on mesoporous silica SBA-15. *J Phys Chem B* 2006, **110**: 24450-24456.
58. Wang J, Tao H, Lu T, *et al.* Adsorption enhanced the oxidase-mimicking catalytic activity of octahedral-shape Mn_3O_4 nanoparticles as a novel colorimetric chemosensor for ultrasensitive and selective detection of arsenic. *J Colloid Interface Sci* 2021, **584**: 114-124.
59. Azzoni CB, Mozzati MC, Galinetto P, *et al.* Thermal stability and structural transition of metastable Mn_5O_8 : in situ micro-Raman study. *Solid State Commun* 1999, **112**: 375-378.
60. Yang LX, Liang Y, Chen H, *et al.* Controlled synthesis of Mn_3O_4 and MnCO_3 in a solvothermal system. *Mater Res Bull* 2009, **44**: 1753-1759.
61. Tsuda M, Arai H, Nemoto Y, *et al.* Electrode performance of sodium and lithium-type romanechite. *J Electrochem Soc* 2003, **150**: A659.

Figures

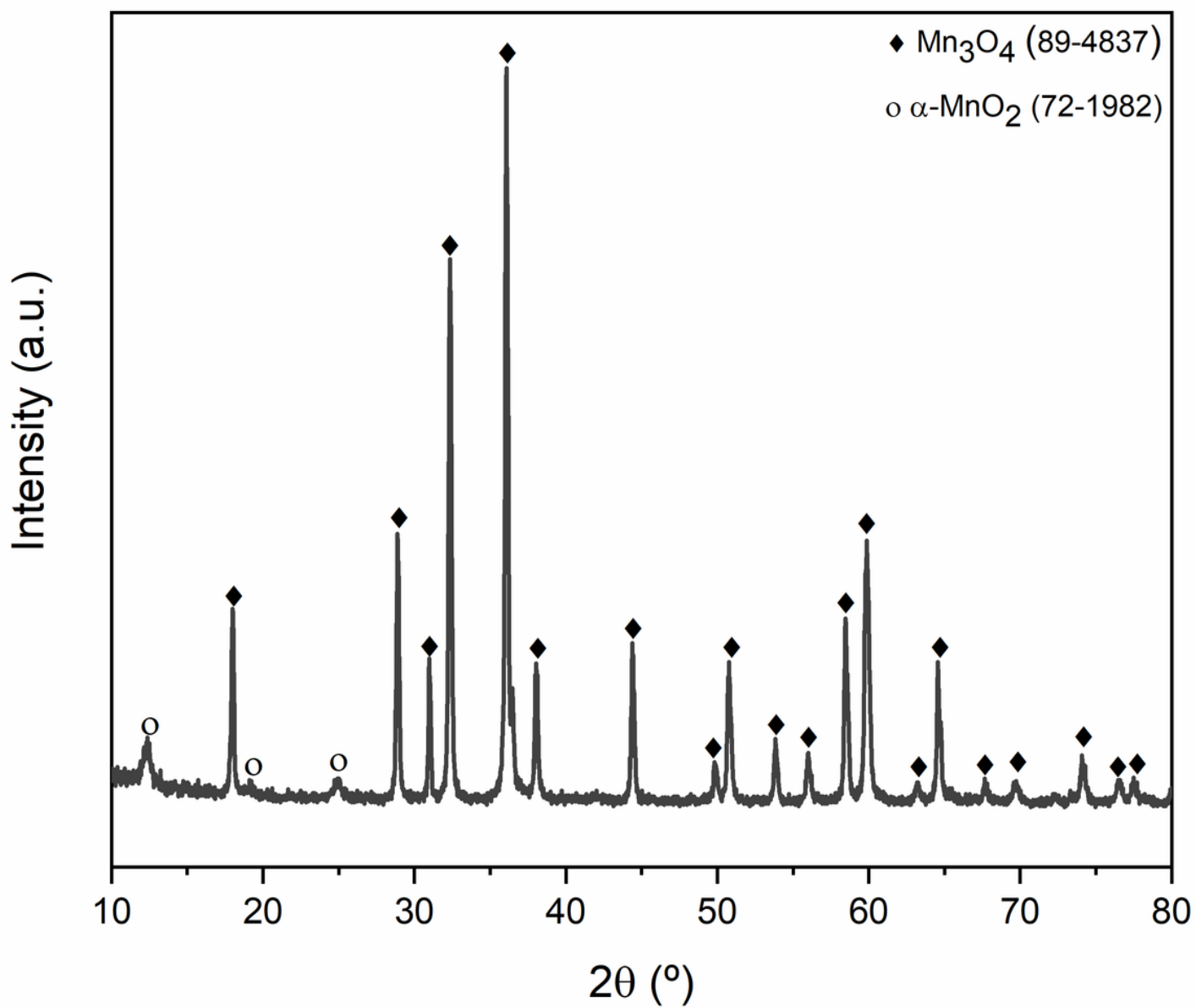


Figure 1

XRD patterns of the MnO sample synthesized via MAH. Assignments: ◆ = tetragonal Mn₃O₄ (JCPDS 89-4837) and ● = tetragonal α-MnO₂ (JCPDS 72-1982).

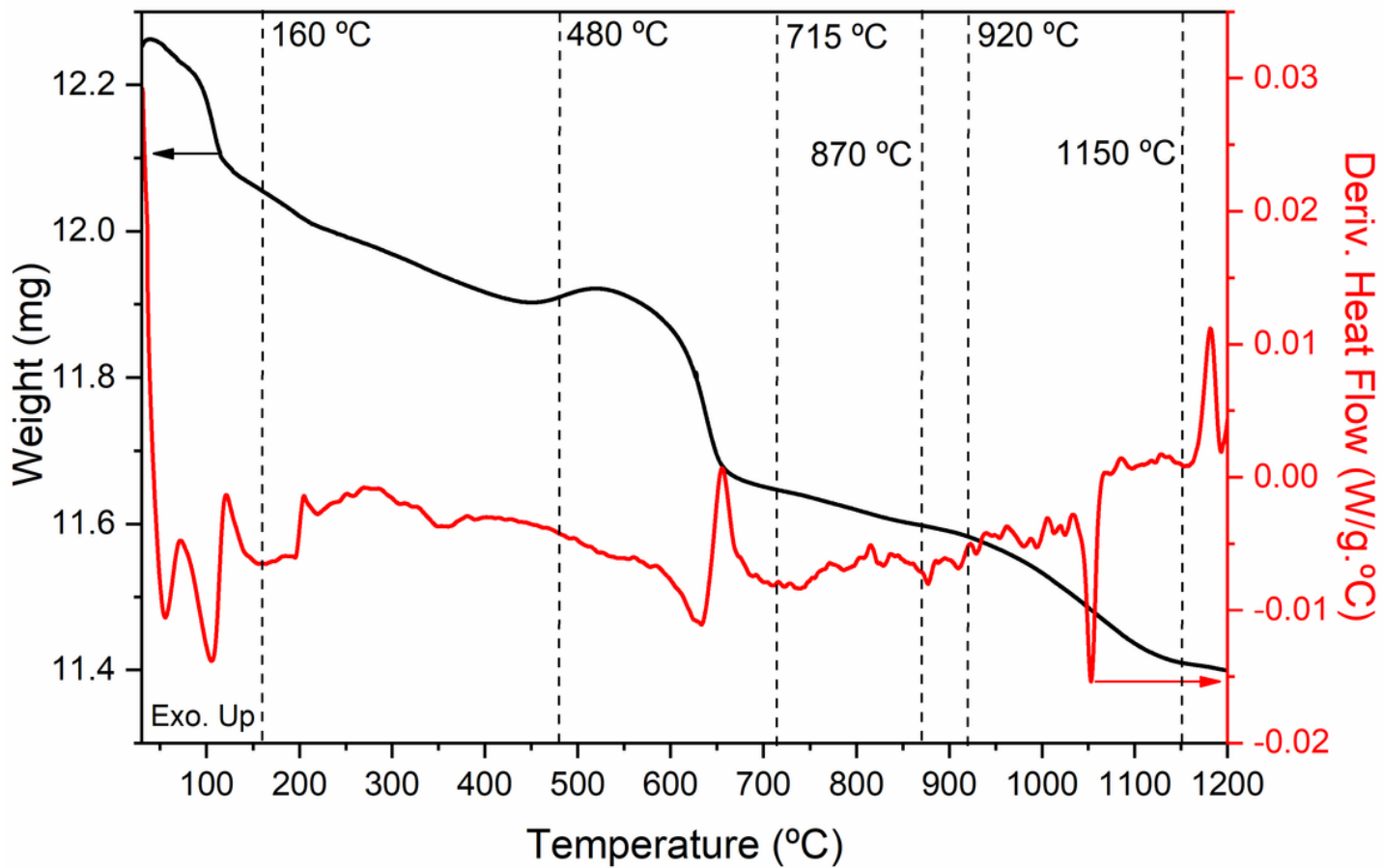


Figure 2

Thermal analysis of the MnO sample synthesized via MAH. The axes for weight change and for the derivative heat flow are indicated. The highlighted temperatures are those where the MnO sample was subsequently heat treated.

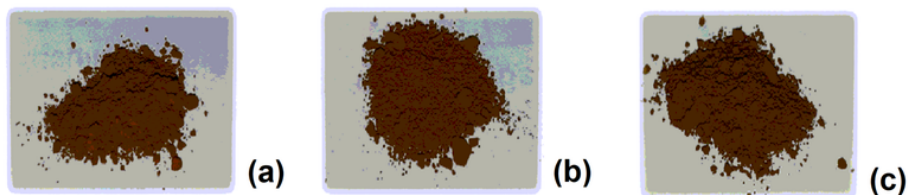
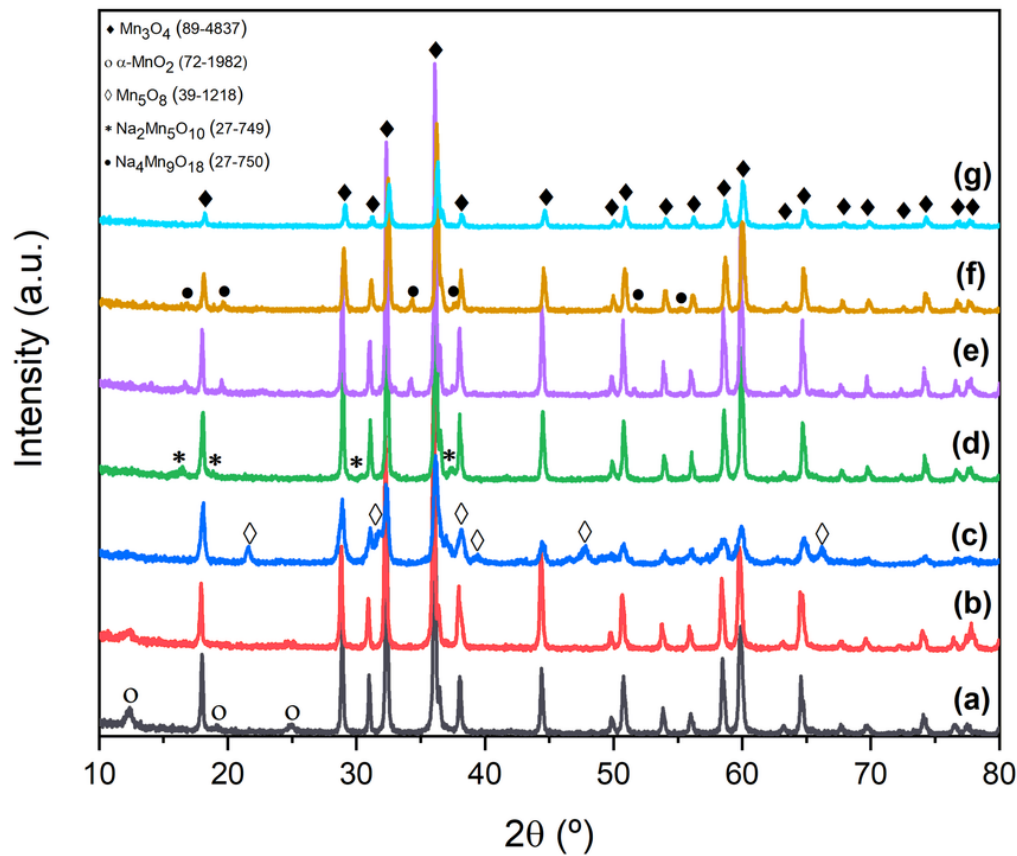
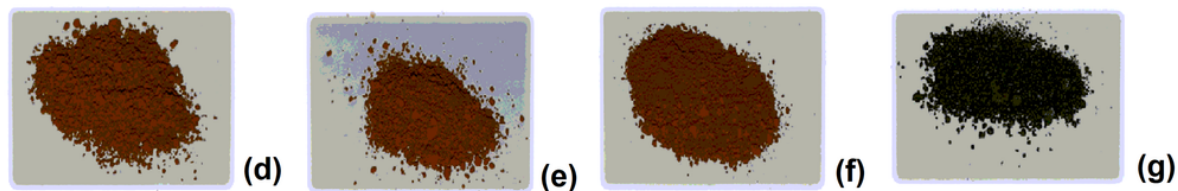


Figure 3

XRD patterns and digital images of the samples (a) MnO, (b) MnO 160 °C, (c) MnO 480 °C, (d) MnO 715 °C, (e) MnO 870 °C, (f) MnO 920 °C e (g) MnO 1150 °C. Assignments: \blacklozenge = tetragonal Mn_3O_4 (JCPDS 89-4837), \bullet = tetragonal $\alpha\text{-MnO}_2$ (JCPDS 72-1982), \diamond = monoclinic Mn_5O_8 (JCPDS 39-1218), \ast monoclinic $\text{Na}_2\text{Mn}_5\text{O}_{10}$ (JCPDS 27-749) and \bullet orthorhombic $\text{Na}_4\text{Mn}_9\text{O}_{18}$ (JCPDS 27-750).

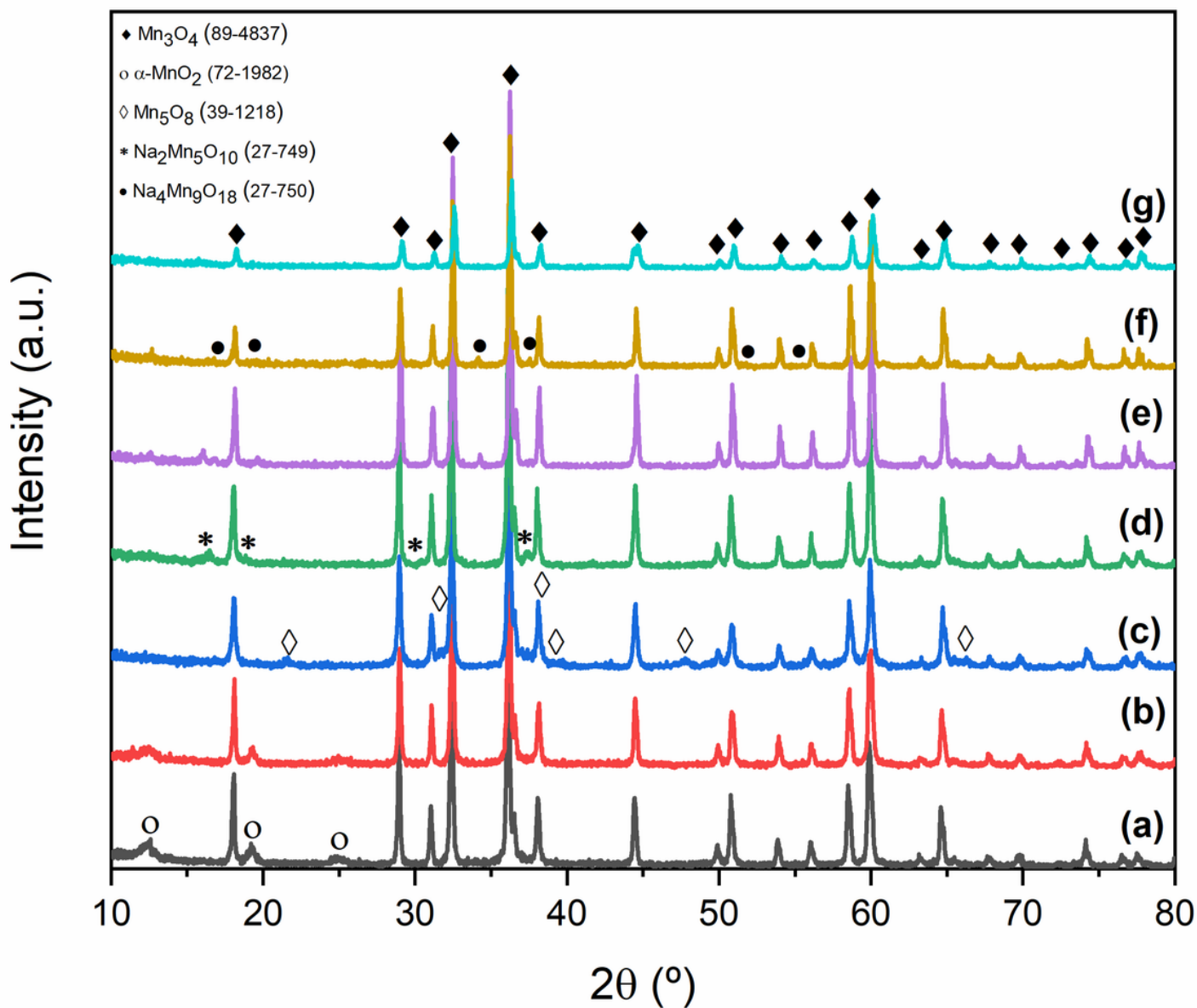


Figure 4

XRD patterns of the replicated samples (a) MnO, (b) MnO 160 °C, (c) MnO 480 °C, (d) MnO 715 °C, (e) MnO 870 °C, (f) MnO 920 °C e (g) MnO 1150 °C. Assignments: \blacklozenge = tetragonal Mn₃O₄ (JCPDS 89-4837), \circ = tetragonal α -MnO₂ (JCPDS 72-1982), \diamond = monoclinic Mn₅O₈ (JCPDS 39-1218), * monoclinic Na₂Mn₅O₁₀ (JCPDS 27-749) and \bullet orthorhombic Na₄Mn₉O₁₈ (JCPDS 27-750).

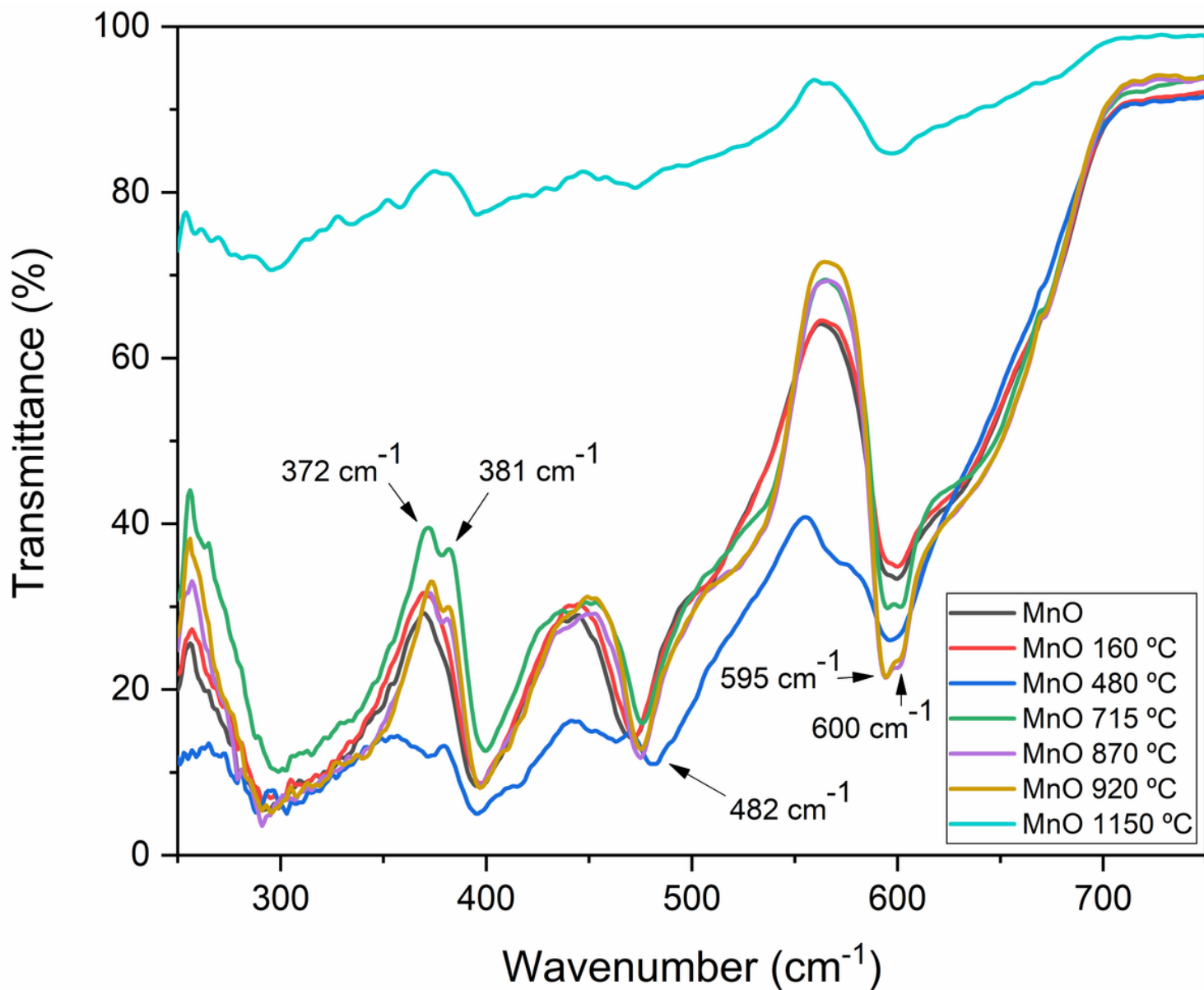


Figure 5

FTIR of MnO, MnO 160 °C, MnO 480 °C, MnO 715 °C, MnO 870 °C, MnO 920 °C and MnO 1150 °C samples.

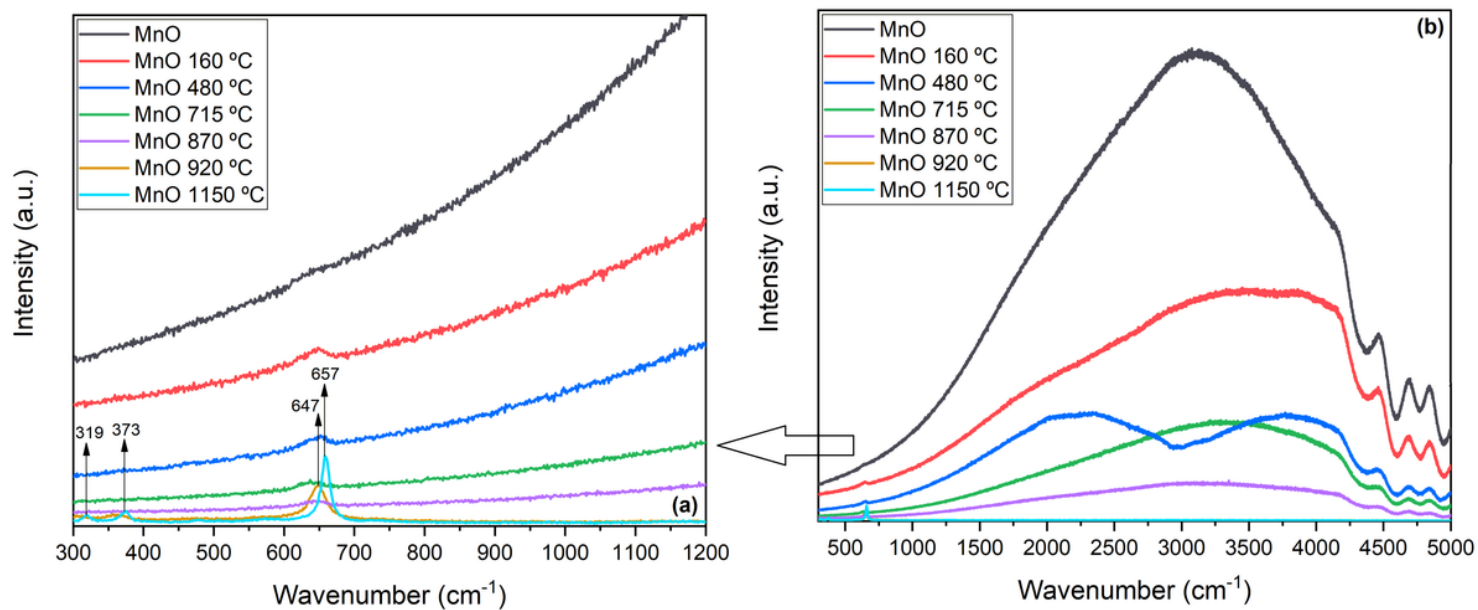


Figure 6

Raman scattering of MnO, MnO 160 °C, MnO 480 °C, MnO 715 °C, MnO 870 °C, MnO 920 °C e MnO 1150 °C samples. (a) 300-1200 cm⁻¹ and (b) 300-5000 cm⁻¹.

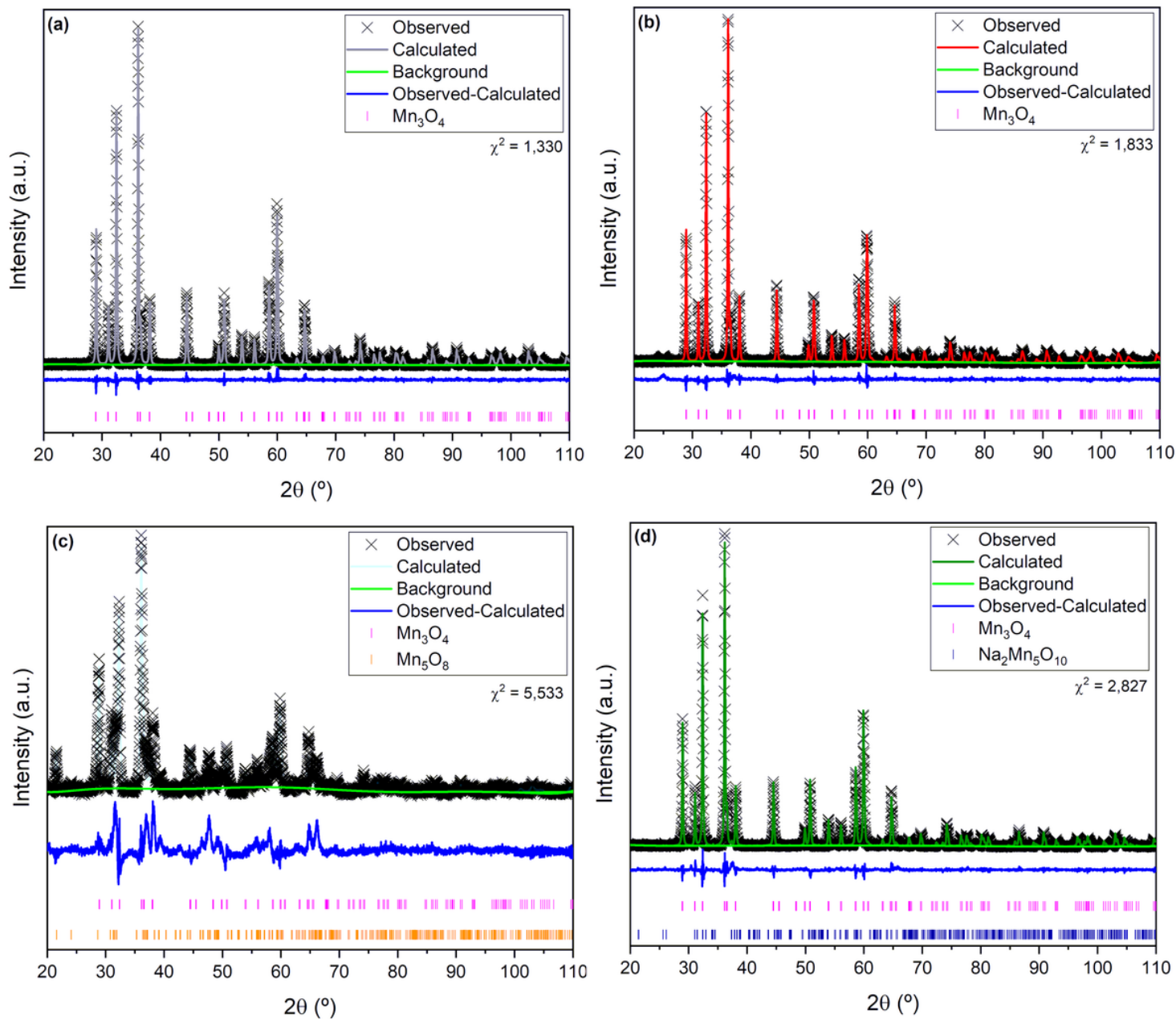


Figure 7

XRD patterns in the structure refinement of the samples (a) MnO, (b) MnO 160 $^{\circ}C$, (c) MnO 480 $^{\circ}C$ and (d) MnO 715 $^{\circ}C$.

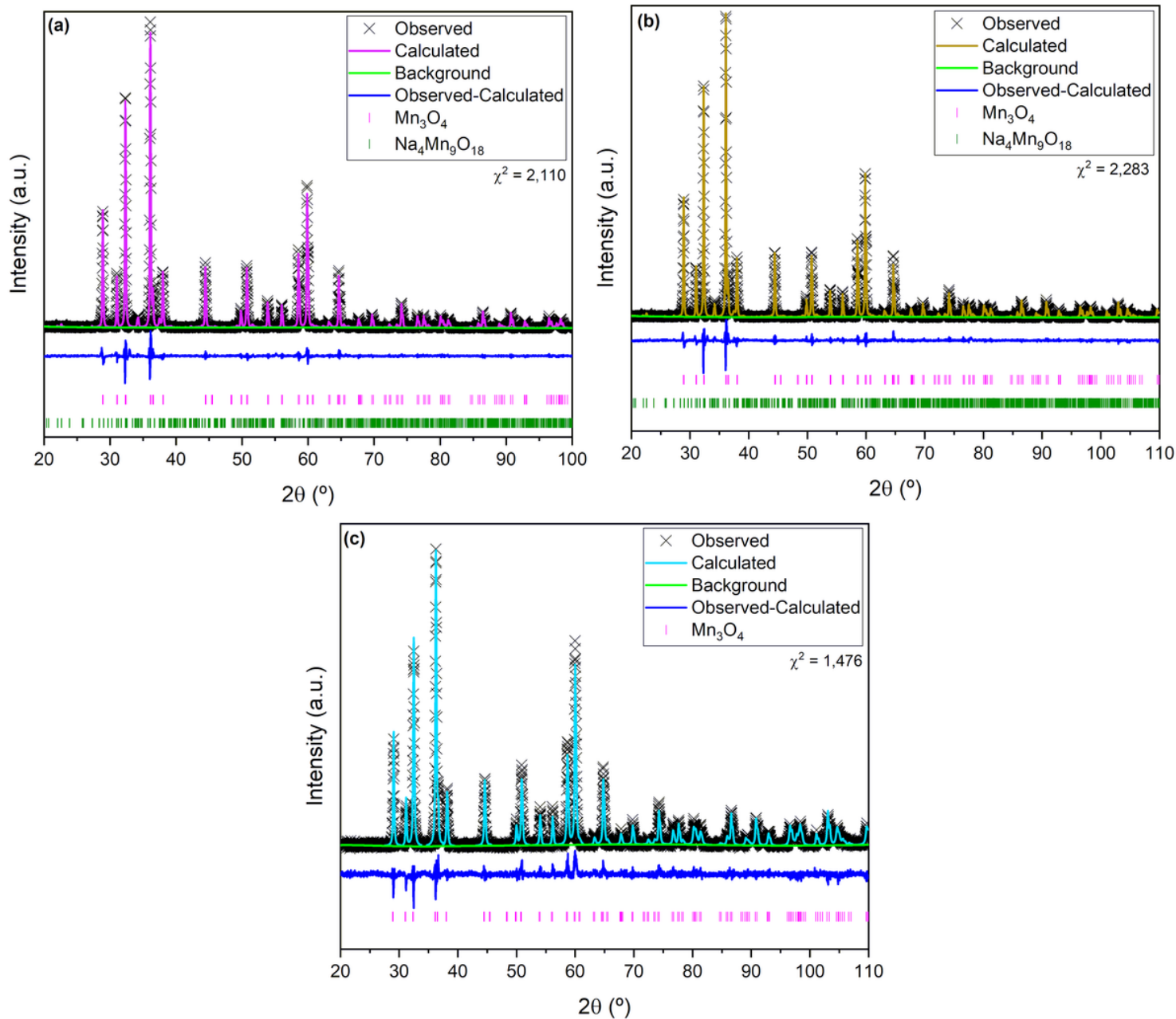


Figure 8

XRD patterns in the structure refinement of the samples (a) MnO 870 $^\circ\text{C}$, (b) MnO 920 $^\circ\text{C}$ and (c) MnO 1150 $^\circ\text{C}$.

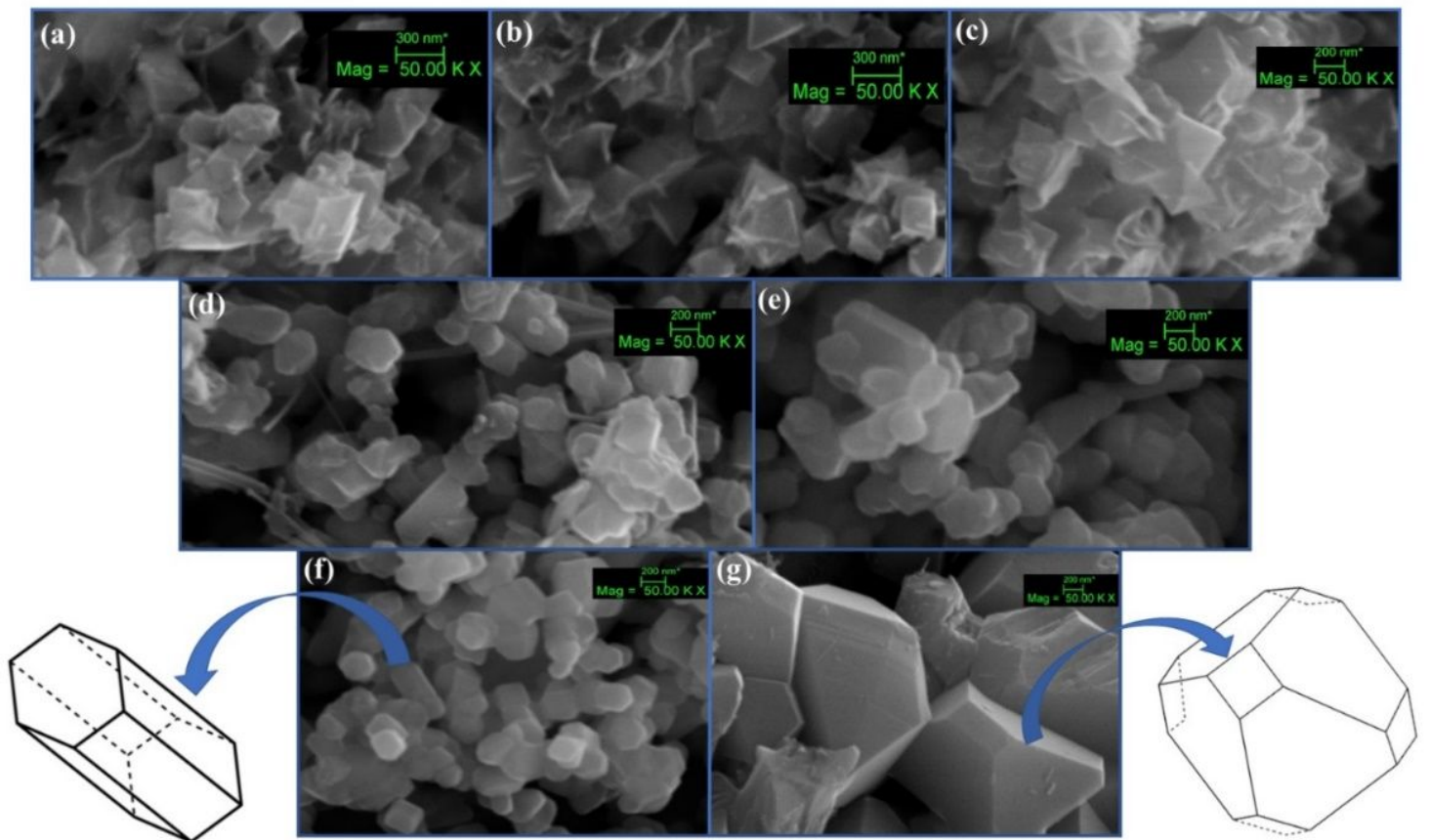


Figure 9

SEM of (a) MnO, (b) MnO 160 °C, (c) MnO 480 °C, (d) MnO 715 °C, (e) MnO 870 °C, (f) MnO 920 °C and (g) MnO 1150 °C samples.